A NEW LOOK AT LOW-RANK RECURRENT NEURAL NETWORKS

Anonymous authors
Paper under double-blind review

ABSTRACT

Low-rank recurrent neural networks (RNNs) have recently gained prominence as a framework for understanding how neural systems solve complex cognitive tasks. However, interpreting these networks remains an important open problem. Here we address this challenge by adopting a view of low-rank RNNs as parametrizing a low-dimensional ordinary differential equation (ODE) using a set of nonlinear basis functions. Through this perspective, which arises from an approach known as the "neural engineering framework", we show that training a low-rank RNN to implement a particular dynamical system can be formalized as least-squares regression in a random basis. This allows us to propose a new method for finding the smallest RNN capable of implementing a dynamical system using a variant of orthogonal matching pursuit. More generally, our perspective clarifies the universal function approximation capabilities of low-rank RNNs (modulo constraints inherited from general RNNs, like only expressing odd symmetric functions in the absence of per neuron inputs/biases), via a geometric interpretation of the network parameters in constructing a flow-field. We further delve into the role of inputs in shaping network dynamics and show that RNNs can produce identical trajectories using a wide variety of static or time-varying dynamics; this highlights the importance of perturbations for inferring dynamics from observed neural trajectories. Finally, we highlight the usefulness of our framework by comparing to RNNs trained using backprop-through-time on neuroscience-inspired tasks, showcasing that our method achieves faster and more accurate learning with smaller networks than gradient-based training.

1 INTRODUCTION

Recurrent neural networks (RNNs) provide a popular tool for analyzing the computational capabilities of neural populations and the mechanisms that enable them to carry out complex cognitive tasks (Miller et al., 2003; Barak, 2017; Mastrogiuseppe & Ostojic, 2018; Schaeffer et al., 2020; Duncker & Sahani, 2021; Dubreuil et al., 2022). A substantial literature focuses on "goal-driven" or "task-driven" approaches in which an RNN is trained to perform a particular cognitive task of interest, and then analyzed to determine what dynamics it uses to solve the task Mante et al. (2013); Sussillo (2014); Kanitscheider & Fiete (2017); Pollock & Jazayeri (2020); Turner et al. (2021). However, both the training and the interpretation of such networks are noteworthy problems of interest.

A wide variety of methods have been proposed for training RNNs on cognitive tasks, including: (1) reservoir computing methods, in which a fixed set of random recurrent weights generate a high-dimensional nonlinear dynamics, and training is applied only to output weights (Jaeger, 2001; Maass et al., 2002); (2) FORCE training, in which a set of random recurrent weights are adjusted using iterative low-rank updates via recursive least-squares Sussillo & Abbott (2009); DePasquale et al. (2018); and (3) methods that adjust all recurrent weights using deep-learning inspired approaches such as back-propagation-through-time (BPTT) Pearlmutter (1990); Sussillo & Barak (2013); Lillicrap & Santoro (2019). Although recent literature has focused primarily on this latter class of gradient-based training methods, they face a variety of challenges, including high computational cost, sensitivity to initialization and hyper-parameters (e.g., learning rate, network size), and susceptibility to vanishing and exploding gradients (Lukoševičius & Jaeger, 2009; Schuessler et al., 2020; Langdon & Engel, 2022; Liu et al., 2023).

Even once they are trained (via any of the above methods), interpreting RNNs to gain insight into task performance remains challenging. Common approaches tend to rely on finding fixed or "slow" points and then using dimensionality reduction methods to visualize projected flow fields Sussillo & Barak (2013); Mante et al. (2013). However, fixed-point finding algorithms are difficult to apply to high-dimensional systems, and it often unclear how accurately low-D projections reflect a network's true dynamics. Previous work has shown that task-trained RNNs with similar performance can nevertheless exhibit different dynamics, raising the question of whether their solutions reveal universal features of task computations (Barak, 2017; Williams et al., 2021).

One recent advance that overcomes many of these difficulties is a theory of low-rank RNNs (Mastrogiuseppe & Ostojic, 2018; Beiran et al., 2021; Dubreuil et al., 2022; Valente et al., 2022). Rather than training a high-dimensional network and then attempting to visualize its behavior using low-D projections, this literature has shown that a wide variety of tasks can be implemented directly in RNNs with intrinsically low dimension, where the dimensionality is set by the rank of the recurrent weight matrix plus input dimensions.

A parallel arm of research has focused on developing methods to embed low-dimensional quantities into high-dimensional network activity (Eliasmith & Anderson, 2003; Stewart, 2012; Abbott et al., 2016; Boerlin et al., 2013; Alemi et al., 2018). Of particular relevance to our work is the Neural Engineering Framework (NEF), which formalizes encoding a stimulus into neuron action potentials using basis functions, and learning an appropriate linear decoder via regression. This learning approach (like FORCE, teacher-forcing methods and neural ODE regression frameworks Sussillo & Abbott (2009); Heinonen et al. (2018); Bhat et al. (2020); Hess et al. (2023)) alleviates gradient based training issues (in cases with known dynamics). Additionally, while Beiran et al. (2021) use such a regression framework, there is no interpretational geometric insight through the use of basis functions.

In this work, we propose an NEF approach to provide an alternate view to low-rank RNNs which addresses interpretabiltiy issues of such models. Specifically, we develop flexible representations through the construction of a randomized basis spanned by the low-dimensional dynamical system. These basis functions are used as regressors to embed a target non-linear ODE in the low-rank RNN using least-squares regression. Second, using this framework we provide empirical and theoretical evidence regarding the representational limits of low-rank RNNs. In particular, we emphasize the necessity of neuron-specific inputs for embedding odd-symmetric dynamics (a constraint also observed in general RNNs) through a geometric interpretation of basis functions. Third, using a variant of orthogonal matching pursuit we derive the smallest RNN that can implement any target ODE. Fourth, we offer novel insights on the influence of *time-varying* inputs in embedding both autonomous and non-autonomous ODEs. Using this, we provide empirical evidence on validating theories such as, how similar trajectories can arise from significantly different dynamical systems, and underscoring the necessity of perturbations for differentiating between these systems. Lastly, we also apply our method to learn simulated ODEs which arise from a neuroscience binary decision making task, thereby proving the effectiveness of our method.

2 Background: recurrent neural networks (RNNs)

Consider a population of d rate-based neurons, with membrane potentials $\mathbf{x} = [x_1, \cdots, x_d]^\top$ and firing rates denoted by $\phi(\mathbf{x}) = [\phi(x_1), \ldots, \phi(x_d)]^\top$, where $\phi(\cdot)$ is a scalar function mapping the membrane potential to firing rate (e.g., sigmoid, hyperbolic tangent, or ReLU). The dynamics of a generic RNN are given by the vector ordinary differential equation and a linear output:

$$\dot{\mathbf{x}} = -\mathbf{x} + J\phi(\mathbf{x}) + I\mathbf{u}(t) \tag{1}$$

$$\mathbf{z} = W\phi(\mathbf{x}), \tag{2}$$

where J is a $d \times d$ recurrent weight matrix, I is a $d \times d_{in}$ matrix of input weights, $\mathbf{u}(t)$ is a d_{in}-dimensional input signal, and $\dot{\mathbf{x}} = [\frac{dx_1}{dt}, \ldots, \frac{dx_d}{dt}]^\top$ denotes the vector of time derivatives of $\mathbf{x}$. To describe behavioral outputs, the model contains a mapping from network activity to an output variable $\mathbf{z}$: where W denotes a $d_{out} \times d$ matrix of readout weights.

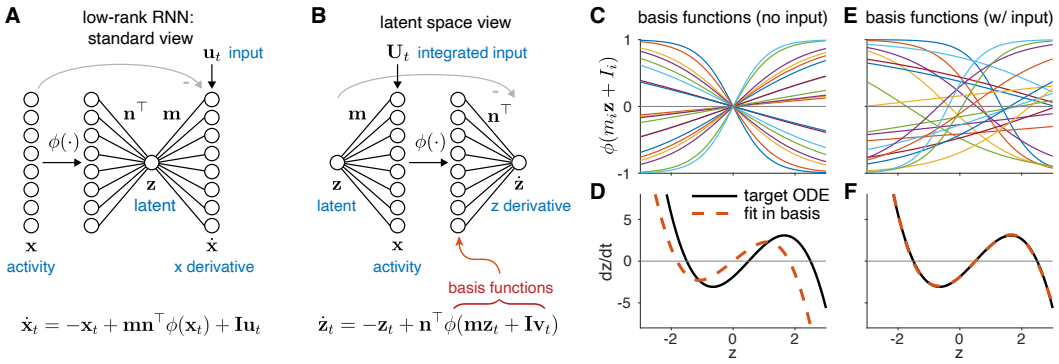

Figure 1: Two equivalent views of low-rank RNNs. **(A)** Standard view of rank-1 RNN with 8 neurons $\mathbf{x}$ and 1 latent dimension $\mathbf{z}$. **(B)** Alternate view of the same network, now framed in terms of the dynamics of latent $\mathbf{z}$. This shows that a low-rank RNN is equivalent to a neural ODE with a single hidden layer (Chen et al., 2018). **(C)** Basis functions obtained by sampling slope parameters $m_i \sim \mathcal{N}(0, 1)$, but without input ($\mathbf{v}_t = 0$). **(D)** Attempting to fit an example ODE using this basis recovers only the odd-symmetric component, since all basis functions are odd symmetric. **(E)** Adding inputs allows basis functions have random horizontal offsets. Here we sampled the input weights $I_i \sim \mathcal{N}(0, 1)$ and set input $\mathbf{v}_t = 1$. (Note that this could also be obtained by using per-neuron "biases"). **(F)** Least squares fitting of $\mathbf{n}$ using the basis from (E) provides good fit to the target ODE.

2.1 Low-rank RNNs

This network model described above becomes a *low-rank RNN* if the recurrent weight matrix J has reduced rank $r < d$, which implies it can be factorized as:

$$J = MN^\top = \sum_{i=1}^{r} \mathbf{m}_i \mathbf{n}_i^\top. \tag{3}$$

Here $\mathbf{m}_i$ and $\mathbf{n}_i$ represent the columns of the $d \times r$ matrices M and N, respectively. In this case, the state vector $\mathbf{x}(t)$ will evolve in a subspace of at most $r + d_{in}$ dimensions (Mastrogiuseppe & Ostojic, 2018; Dubreuil et al., 2022). Activity in the remaining dimensions will decay to zero due to the decay term $(-\mathbf{x})$ in (eq. 1).

In this setting, the network state $\mathbf{x}$ can be re-written as

$$\mathbf{x}(t) = M\boldsymbol{\kappa}(t) + I\mathbf{v}(t), \tag{4}$$

where $\boldsymbol{\kappa}$ is a so-called "latent" vector representing activity in the r-dimensional recurrent subspace, and $\mathbf{v}(t)$ represents the low-pass filtered input signals $\mathbf{u}(t)$ Dubreuil et al. (2022); Valente et al. (2022). Finally, the low-dimensional recurrent dynamics can be represented in terms of a differential equation: $\dot{\boldsymbol{\kappa}} = F(\boldsymbol{\kappa}, \mathbf{u})$, where F is a nonlinear function of the latent state $\boldsymbol{\kappa}$ and input $\mathbf{u}$.

3 An alternate view of low-rank RNNs

In the framework described above, training a low-rank RNN to produce a desired output $\mathbf{z}(t)$ from an input $\mathbf{u}(t)$ requires learning the model parameters $\{N, M, I, W\}$, which is typically carried out using back-propagation through time Valente et al. (2022). Here we present a different approach to low-rank RNNs, which provides a more intuitive portrait of the network's dynamical capabilities.

We begin by considering the problem of embedding an arbitrary low-dimensional dynamical system into a low-rank RNN. Specifically, suppose we wish to set the model parameters so that $\mathbf{z}$ obeys the dynamics of an particular nonlinear ODE:

$$\dot{\mathbf{z}} = g(\mathbf{z}), \tag{5}$$

for some function g. We will then identify this output with the latent vector defining the network's activity in the recurrent subspace: $\mathbf{z}(t) \triangleq \boldsymbol{\kappa}(t)$. This implies that the dimensionality of the output is

equal to the rank of the network, $r = d_{out}$, and constrains the output weights to be the projection operator onto the column space of M, that is, $W = M(M^\top M)^{-1}$. We are then left with the problem of setting the weights M, N, and I so that the latent vector, which we now refer to as $\mathbf{z}(t)$, evolves according to (eq. 5). (Note however the model output need match the dimensionality of the latent variable; in cases where desired output is lower-dimensional than $\mathbf{z}$, the output can be expressed as $\mathbf{z}' = A\mathbf{z}$, where A is some fixed matrix of output weights that, for example, selects only one component of $\mathbf{z}$.)

For simplicity, we begin with the case of a scalar $\mathbf{z}$. This corresponds to an RNN with rank-1 recurrent weight matrix $J = \mathbf{m}\mathbf{n}^\top$, which is simply an outer product of weight vectors $\mathbf{m}$ and $\mathbf{n}$. Assume that the input is also scalar, and that the input vector I is orthogonal to $\mathbf{m}$ (although we can relax this constraint later). Following previous work (Beiran et al., 2021; Dubreuil et al., 2022; Valente et al., 2022) (eq. 4), the network state can be decomposed as a time-varying linear combination of $\mathbf{m}$ and I:

$$\mathbf{x}(t) = \mathbf{m}\mathbf{z}(t) + I\mathbf{v}(t), \tag{6}$$

where $\mathbf{v}(t)$ represents the low-pass filtered input, resulting from the linear dynamical system $\dot{\mathbf{v}} = -\mathbf{v} + \mathbf{u}(t)$. The fact that $\mathbf{m}$ and I are orthogonal means that we can write the dynamics governing the latent variable explicitly as:

$$\dot{\mathbf{z}} = -\mathbf{z} + \mathbf{n}^\top \phi(\mathbf{m}\mathbf{z} + I\mathbf{v}(t)) \tag{7}$$

a result shown previously in Valente et al. (2022), and which is schematized in Fig. 1. Given this expression, our goal of embedding an arbitrary ODE $\dot{\mathbf{z}} = g(\mathbf{z})$ into the network can be viewed as setting the model parameters so that

$$g(\mathbf{z}) + \mathbf{z} \;\approx\; \mathbf{n}^\top \phi(\mathbf{m}\mathbf{z} + I\mathbf{v}(t)) \tag{8}$$

To achieve this, note that the right-hand-side can be viewed as a linear combination of terms $\phi(m_i\mathbf{z} + I_i\mathbf{v}(t))$ with weights n_i, for $i \in \{1, \ldots, d\}$. Each of these terms can be viewed as a basis function in $\mathbf{z}$ for representing the target $g(\mathbf{z}) + \mathbf{z}$. More specifically, if ϕ is the hyperbolic tangent function, each such term is a shifted, scaled $\tanh$ function in $\mathbf{z}$, where m_i is the slope and $I_i v(t)$ is the offset. This means that we can view the problem of embedding $g(\mathbf{z})$ into a low-rank RNN as the problem of setting $\mathbf{m}$ and I to build an appropriate set of basis functions, and setting $\mathbf{n}$ so that the linear combination of basis functions approximates $g(\mathbf{z}) + \mathbf{z}$. This approach formalizes the connection between low-rank RNNs and the NEF (Eliasmith & Anderson, 2003; Barak & Romani, 2021), and shows that a low-rank RNN corresponds to a neural ODE with a single hidden layer (Chen et al., 2018; Pellegrino et al., 2023; Pals et al., 2024).

Already, this perspective makes an important limitation clear: if the inputs $\mathbf{v}(t)$ are zero, the basis functions are all odd-symmetric (that is, $g(m_i\mathbf{z}) = -g(-m_i\mathbf{z})$ for all $\mathbf{z}$), crossing the origin only at zero. (see Fig. 1C). Because $-\mathbf{z}$ is also odd-symmetric, and the linear combination of odd-symmetric functions is odd-symmetric, this means that in the absence of inputs, the network can only capture the odd-symmetric component of $g(\mathbf{z})$. A low-rank RNN is therefore not a universal approximator unless it has inputs, or equivalently, different biases or offsets to each neuron (similar to general RNNs). If the ϕ is instead taken to be ReLu, the problem is even more severe: each basis function is a linear function with non-zero slope on either $\mathbf{z} > 0$ or $\mathbf{z} < 0$. Thus the network can only approximate $g(\mathbf{z})$ that are piecewise linear functions broken at the origin. (See SI Fig. SI-1).

If we set the filtered input to be the constant $\mathbf{v} = 1$, we see that the problem of embedding an arbitrary ODE in a low-rank RNN amounts to fitting the ODE in a basis of shifted and scaled basis functions in $\mathbf{z}$. To achieve this, we propose to sample the scales (elements of $\mathbf{m}$) and offsets (elements of I) to obtain a random basis, and then fit $\mathbf{n}$ by least-squares regression, namely:

$$\hat{\mathbf{n}} = (\phi(\mathbf{z}_{grid}\mathbf{m}^\top + I^\top)^\top \phi(\mathbf{z}_{grid}\mathbf{m}^\top + I^\top))^{-1} \phi(\mathbf{z}_{grid}\mathbf{m}^\top + I^\top)^\top \big(g(\mathbf{z}_{grid}) + \mathbf{z}_{grid}\big), \tag{9}$$

where $\mathbf{z}_{grid}$ denotes a grid of points at which we wish to fit $g(\mathbf{z})$. Note that we could use weighted least squares if we care more about accurately approximating certain regions of $g(\mathbf{z})$, or add a small ridge penalty if the design matrix (whose columns are given by the basis functions evaluated at $\mathbf{z}_{grid}$) is ill-conditioned.

Fig. 1 shows an illustration of this approach for an example ODE, here chosen to be a cubic polynomial with two stable fixed points and one unstable fixed point. Note that the network cannot approximate $g(\mathbf{z})$ when the inputs are set to zero (Fig. 1C-D), but can do so with near-perfect accuracy when both the $\mathbf{m}$ vector and the (constant) inputs $I\mathbf{v}$ are drawn from a Gaussian distribution (Fig. 1E-F)).

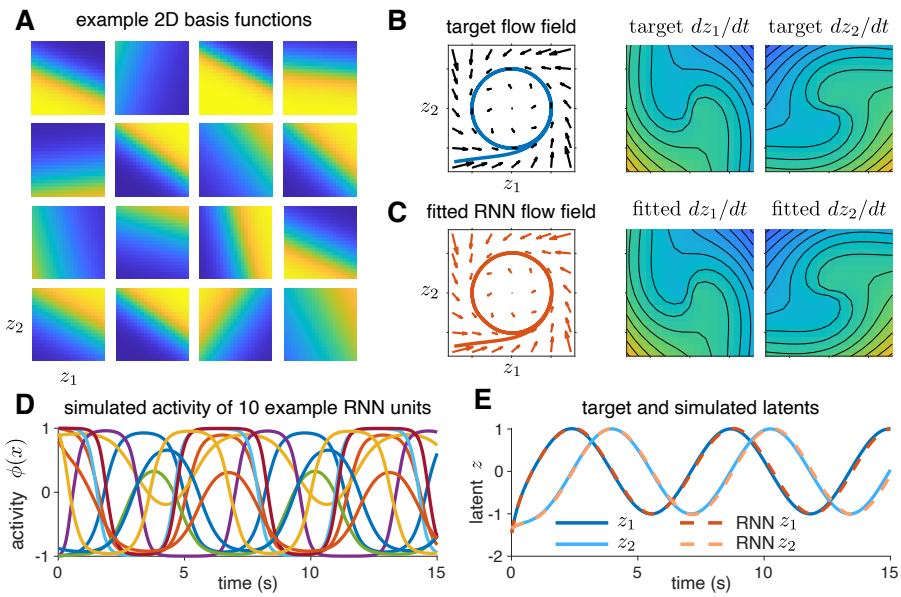

Figure 2: Embedding a 2-dimensional nonlinear ODE into a rank-2 RNN. **(A)** Example basis functions obtained by sampling M and I coefficients from a zero-mean Gaussian, producing randomly oriented, scaled, and shifted hyperbolic tangent functions. **(B)** A target two-dimensional nonlinear dynamical system, containing a stable limit cycle on a circle of radius one, represented as a flow field (left), or by its component functions $g_1(\mathbf{z}) = \frac{dz_1}{dt}$ and $g_2(\mathbf{z}) = \frac{dz_2}{dt}$ (right). **(C)** Least squares fitting of weight vectors $\mathbf{n}_1$ and $\mathbf{n}_2$ produces a near perfect match to the target flow field, and functions g_1 and g_2. **(D)** Output firing rates $phi(x_i)$ for 10 example units (i.e $i \in \{1, \ldots, 10\}$) during the red example trajectory shown in panel C. **(E)** Simulated trajectories from the true ODE (blue trace in panel B) and latent variable of the fitted RNN (red trace from panel C), plotted as a function of time, showing good agreement between the target ODE and the RNN output. Note that fitting was closed-form, and did not require backprop-through-time.

3.1 Multi-dimensional dynamical systems

We can apply this same regression-based approach to higher-dimensional nonlinear dynamical systems, where rank $r = \dim(\mathbf{z}) > 1$. In two dimensions, the basis functions are given by $\phi(m_{1i}z_1 + m_{2i}z_2 + I_i)$, which are scaled, shifted $\tanh$ functions with a random orientation (see Fig. 2A). Approximating a 2D dynamical system with a rank-2 RNN can then be written as the problem of fitting two different nonlinear functions $g_1(\mathbf{z})$ and $g_2(\mathbf{z})$ using two different linear combinations of the same 2D basis functions:

$$g(\mathbf{z}) = \begin{bmatrix} g_1(\mathbf{z}) \\ g_2(\mathbf{z}) \end{bmatrix} \approx -\begin{bmatrix} z_1 \\ z_2 \end{bmatrix} + \begin{bmatrix} \mathbf{n}_1^\top \phi(M\mathbf{z} + I) \\ \mathbf{n}_2^\top \phi(M\mathbf{z} + I) \end{bmatrix}, \tag{10}$$

where $M = [\mathbf{m}_1 \mathbf{m}_2]$ is a $d \times 2$ matrix whose columns define the slope and orientation of each basis function, I is once again a column vector of offsets, and we have assumed constant input ($\mathbf{v} = 1$). Note once again that if we do not include inputs, the basis functions are all radially odd-symmetric around the origin. Thus, once again, the RNN will only be able to capture radially odd-symmetric $g(\mathbf{z})$, and is not a universal approximator unless we include nonzero offsets $I\mathbf{v} \neq 0$.

To embed a given multi-dimensional ODE $g(\mathbf{z})$ into a low-rank RNN, we once again generate a random basis by sampling the elements of $M \in \mathbb{R}^{d \times 2}$ and $I \in \mathbb{R}^d$ from a Gaussian distribution. The problem factorizes into learning each column vector $\mathbf{n}_i$ for each dimension of the g, we have:

$$\hat{\mathbf{n}}_i = (\phi(Z_{grid}M^\top + I^\top)^\top \phi(Z_{grid}M^\top + I^\top))^{-1} \phi(Z_{grid}M^\top + I^\top)^\top \big(g(Z_{grid}) + Z_{grid}\big), \tag{11}$$

for $i = 1, 2$. This differs from the 1D case above only in that Z_{grid} is now a r-column matrix of grid points, where each row contains the coordinates of a single point in $\mathbf{z}$. Note that these grid

points need not be uniformly sampled; we could sample them from an arbitrary distribution, or use a collection of points from simulating the ODE from a variety of starting points.

Fig. 2 shows an application to an example 2-dimensional nonlinear ODE, in this case containing a stable limit cycle. Note that this 2D system is highly nonlinear and not radially odd-symmetric, so once again (Section A.2), embedding the system in a low-rank RNN fails if we do not include inputs (or per-neuron biases).

4 FINDING THE SMALLEST RNN FOR A GIVEN DYNAMICAL SYSTEM

We now turn to the question of finding the smallest RNN that can accurately implement a known nonlinear dynamical system, $g(\mathbf{z})$, focusing on a scalar z. In other words we aim to determine the minimum number of neurons ($d' << d$) needed by the network to approximate the function $g(\mathbf{z})$. Our goal is thus to solve an optimization problem that imposes a sparsity constraint on the dimensionality of our basis set $B(\mathbf{m}, I)$, while still solving for an appropriate linear weighting $\mathbf{n}$.

More formally, this implies selecting the best d' entries from $B(\mathbf{m}, I)$, to create a basis:

$$B_{d'}(\mathbf{m}, I) = \begin{bmatrix} \phi(m_{i_1}\mathbf{z} + I_{i_1}) \\ \phi(m_{i_2}\mathbf{z} + I_{i_2}) \\ \vdots \\ \phi(m_{i_{d'}}\mathbf{z} + I_{i_{d'}}) \end{bmatrix}, \quad \text{where } \{i_1, i_2, \ldots, i_{d'}\} \subseteq \{1, 2, \ldots, d\}.$$

Then, a linear weighting $[n_0 \ \mathbf{n}']$ is learned using least squares regression, where:

$$g(\mathbf{z}) \ \approx \ -n_0 * z + \mathbf{n}'^{\top} B_{d'}(\mathbf{m}, I) \quad \text{where } \{\mathbf{n}' = 1 \times d' \text{ vector}\} \tag{12}$$

To achieve the desired optimization of approximating $g(z)$, we begin with a large enough $B(\mathbf{m}, I)$ obtained by sampling from a uniform grid of values for $\mathbf{m}, I$. We then follow an iterative approach, wherein at each iteration t, we greedily pick a basis function i_j that has the highest alignment to the current residual estimate of $g(\mathbf{z})$. This can be observed as an adaptation of the well-established orthogonal matching pursuit (OMP) framework. A more detailed description of this process is provided below in Algorithm 1. It is worth noting, changing the original basis set $B(\mathbf{m}, I)$ to $B'(\mathbf{m}, I)$, could result in the algorithm converging to a different minima (global minima in $B'(\mathbf{m}, I)$ could be different from global minima in $B(\mathbf{m}, I)$). However, if the basis sets are equivalent we observe similar performance across simulations (Fig SI-9)).

Algorithm 1 OMP for finding smallest RNN

1: Select a grid of values $\mathbf{z}$.
2: Create global basis set $\boldsymbol{B}$ using uniformly sampled $\mathbf{m}, I$ values.
3: Initialize n weights using linear decay term only: $n_0 = -(\mathbf{z}^{\top}\mathbf{z})^{-1}\mathbf{z}^{\top}g(\mathbf{z})$.
4: Initialize residual: $r_0 = g(\mathbf{z}) - n_0 * (-\mathbf{z})$
5: At each iteration t:
   1. Find basis vector with highest correlation with residual: $i_t = \arg\max_i ||\mathbf{B}_i^T \mathbf{r}_{t-1}||$
   2. Add new entry to the solution basis, $B_t \leftarrow \boldsymbol{B}_i$
   3. Solve to find new linear weights $\mathbf{n}'_t$ using Eqn 9
   4. Compute the updated residual: $r_t = g(\mathbf{z}) - \mathbf{n}'^{\top}_t B_t$
   5. Check for termination based on a predefined sparsity threshold $d' = \text{len}(B_t)$

In Fig 3, we apply this method to a simulated 1D ODE, with two stable fixed points and one unstable fixed point. The first row shows the greedily-added basis functions, multiplied by their corresponding learned linear weightings. The bottom row shows their linear combination against the true underlying ODE. Through this iterative process, we observe with just 5 neurons our network almost perfectly reconstructs the target ODE.

It is worth noting, previous work (e.g., Luo et al. (2023); Valente et al. (2022)) have similar dynamics which are learned using BPTT with much larger networks (typically 512 neurons). Our method instead provides an empirical framework to find the minimum number of neurons needed to fit dynamics within estimated margins of error. Furthermore, we believe this could be used to provide insights on hyper-parameter values (such as number of neurons) for neural ODE models or other artificial networks.

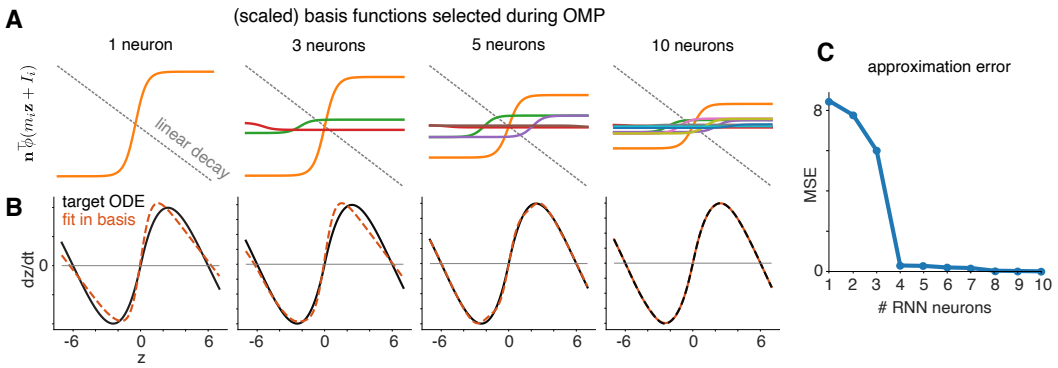

Figure 3: Finding the smallest RNN for a particular nonlinear dynamical system using orthogonal matching pursuit (OMP). **(A)** Scaled basis functions selected after 1, 3, 5, and 10 iterations of OMP, along with the linear decay term $-x$ for an example ODE (shown below). **(B)** Target ODE (black) and RNN fit after each step of OMP. **(C)** Mean squared error (MSE) between target ODE and RNN approximation as a function of the number of RNN neurons added by OMP.

5 New insights into the role of input dynamics

In Sec. 3, we demonstrated the importance of the presence of inputs in basis functions, $B(\mathbf{m}, I) = \phi(\mathbf{m}\mathbf{z} + I\mathbf{v}(t))$. Now, we highlight the influence of the type of inputs (constant or time-varying), in representing arbitrary ODEs. Specifically, our framework so far shows how autonomous ODEs ($g(\mathbf{z})$) are embedded via constant filtered inputs represented as $v = 1$, that do not evolve over time. Here we extend our framework to embed non-autonomous ODEs ($g(\mathbf{z}, t)$) by introducing a dynamical system that governs the evolution of $\mathbf{v}(t)$.

Recent work has suggested an identifiability issue in uncovering underlying low-dimensional dynamics from high-dimensional neural activity, however the role inputs play in this hasn't been explored (Turner et al., 2021; Langdon & Engel, 2022; Liu et al., 2023; Qian et al., 2024). Furthermore, previous work on time varying inputs (Rajan et al., 2016; Remington et al., 2018; Galgali et al., 2023a) has focused primarily on whether observed trajectories were *input driven* or *dynamics driven* . We note here that this latter category can be subdivided into cases where the dynamics themselves are fixed in time or fluctuating due to inputs.

In Fig. 4, we illustrate using our framework to train low-rank RNNs that produce an identical trajectories (blue, red lines in the bottom row) through vastly different dynamical systems (quiver plots in bottom row). In all cases shown, the input dimension I is orthogonal to the dynamics subspace $\mathbf{m}$. Specifically, we demonstrate the following cases:

1. Autonomous ODE: Following the general treatment in Sec. 3 above, we embed an ODE of the form $\dot{\mathbf{z}} = g(\mathbf{z})$. The quiver plot (bottom row of panel A) represents the autonomous ODE flow-field illustrated through arrows of the same length across time, for each value of $\mathbf{z}$. Note, this embedding is achieved through inputs that are fixed in time ($\mathbf{v} = 1$). Additionally in the bottom row of panel A, the true trajectory (blue - computed using Euler integration), and the low-rank RNN (red - trained using Eqn 9), both start at the unstable fixed point ($\mathbf{z} = -6$), and eventually converge to the stable fixed point ($\mathbf{z} = +6$). The almost perfect overlap indicates the efficacy of our method.

2. Non-Autonomous ODE: In panels B,C,D we embed *time-varying* dynamics of various kinds into different low-rank RNNs. Our training objective was to create time-varying flow fields that produce a trajectory identical to the autonomous ODE case. The existence of time-varying dynamics can be observed by noting arrows of different lengths across time bins (i.e each row of quiver plot).
We first discuss how to embed such dynamics into the low-rank RNN. Intuitively, because the dynamic being approximated represents a different function over time, the basis functions also need to evolve in time. To achieve this embedding, we modeled inputs $\mathbf{v}(t)$ with an exponential decay given by $\dot{\mathbf{v}} = -\mathbf{v}$. This decay results in time-varying basis functions, as different $\mathbf{v}(t)$ values are computed at each Euler time-step when defining $\phi(\mathbf{m}\mathbf{z} + I\mathbf{v}(t))$.

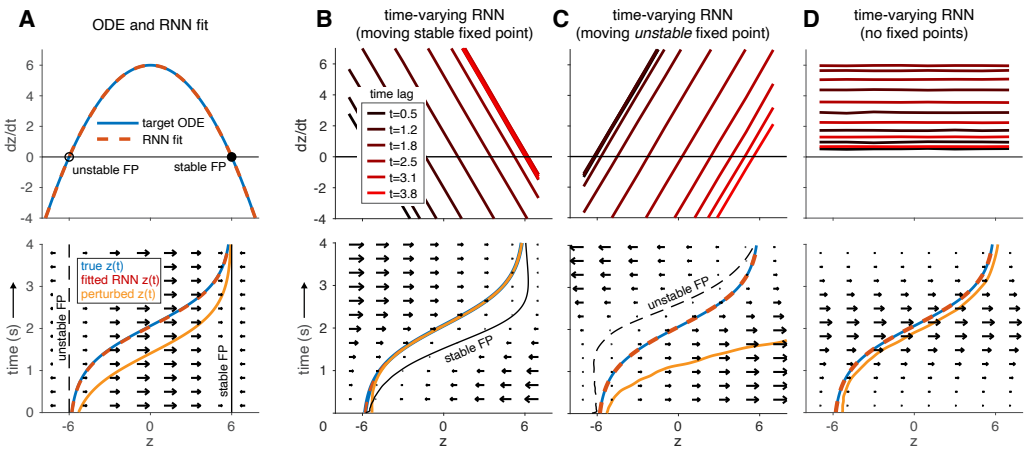

Figure 4: Creating indistinguishable time-varying dynamical systems with time-varying inputs. We show four different time-varying dynamical systems that give rise to the same (blue) target trajectory. **(A)** Top: we defined a target ODE defined by an inverted quadratic function (top), then embedded into an RNN with constant input (following the methods in Sec. 3). Bottom: we then simulated a trajectory that starts just right of the unstable fixed point and converges to the stable fixed point. Here the flow field dynamics do not vary in time. A perturbed input into the RNN (orange) follows the same trajectory, but shifted downward (earlier) in time. **(B)** We trained an RNN to produce a dynamic flow field using time varying basis functions, whose offsets shifted in time after clamping on an input $\mathbf{u}$ at time zero. Here we set the target to be a time-varying linear dynamical system with a single stable fixed point that moved from left to right. Note that the RNN latent (red) still follows the target trajectory (blue). However, the same perturbation shown in A now converges back to the target trajectory. **(C)** Network trained to produce the same target trajectory using a moving *unstable* fixed point. **(D)** Network trained to produce the same target trajectory using no fixed points. Note however that the trajectory arising from a perturbed initial point (yellow) varies wildly across these models.

Below, we expand on the specific dynamical system governing ODEs that can be approximated using such time-varying basis functions.

1. **Moving fixed points**: As already highlighted, the dynamical system of the target ODE is of the form $\dot{\mathbf{z}} = g(\mathbf{z}, t)$. Panels B, C present specific cases, where this dynamic represents an underlying flow-field which arises due to the diffusion of a single stable or unstable fixed point.
   In other words, our target ODE represents the trajectory of a moving fixed point, modelled through a linear dynamic term in $\mathbf{z}$ -
   $$\dot{\mathbf{z}} = g(\mathbf{z}(t') - \alpha * (\mathbf{z}' - \mathbf{z}(t')) - \mathbf{z}' \tag{13}$$
   The above equation clearly highlights the systems' state depends on both $\{\mathbf{z}', t'\}$, representing a coarse spacing and a corresponding Euler time bin respectively. First, the term $\alpha * (\mathbf{z}' - \mathbf{z}(t'))$ introduces a linear time-varying correction which moves the fixed point of this system $\mathbf{z}'$ to $\mathbf{z}(t')$ with a rate α, as shown in the top rows. Second, α must be positive for panel B (to move a single *stable* fixed point), and negative for panel C (to move a single *unstable* fixed point). Third, while the fixed point dynamic described above is linear, the system still evolves non-linearly due to the function g, as shown by the quiver plots. Lastly, in the absence of these dynamics the system decays to the fixed point defined by $\mathbf{z}'$.
2. **No fixed points**: Similar to the moving fixed point case, we can define a system with no fixed points during the movement from -6 to +6. In this case, the target ODE is defined by the non-linear evolution of $\mathbf{z}(t)$ with a time-invariant shift given as
   $$\dot{\mathbf{z}} = g(\mathbf{z}(t')) - \mathbf{z}' \tag{14}$$

In the bottom row of panels B,C,D the true trajectory (blue) and RNN approximated trajectory (red) overlap. Critically, they are all identical, and in fact match the trajectories observed in the bottom row

of panel A. However, as discussed above, they all represent dramatically different target flow-fields, also showcased via their quiver plots.

Our results provide insight into how non-autonomous dynamics can be embedded into low-rank RNNs through time-varying inputs. It is worth noting that most current methods typically interpret low-dimensional dynamics post-training. One specific method that has gained popularity is the zero-finding method, which relies on finding fixed points (Sussillo & Barak, 2013; Smith et al., 2021). Our discussion on non-autonomous dynamics suggests, how similar trajectories can be observed in the presence of dynamical fixed points/ no fixed points at all. This presents a possible failure mode for such techniques. Additionally, we consider the effects of perturbations in the initial point (orange line in bottom row) for these different systems. As observed, while the learned RNN trajectory (black) is identical across all panels, small perturbations in the initial point lead to wildly different trajectories in different models, validating that observations of fixed trajectories are generally not sufficient to uniquely identify the underlying dynamical system Galgali et al. (2023b).

6 Comparison with BPTT for neuroscience tasks

Finally, we apply our framework on two neuroscience inspired tasks (Wong & Wang, 2006; Sussillo & Barak, 2013; Luo et al., 2023) and compare our networks against RNN models trained with backprop-through time. Specifically, we implement:

1. **3-bit flip-flop task**: The network receives a series of bits (-1 or +1) in 3 registers, and must store the polarity of the most recent bit in each register (Sussillo & Barak, 2013).
2. **Binary decision-making**: Following previous literature, we model a sensory evidence accumulation task using bi-stable attractors (Wong & Wang, 2006). Sensory inputs drive the system from an unstable fixed point towards one of two stable fixed points, each associated with a different choice (see Appendix B for details).

In Sec. 4, we find the smallest low-rank ($r = 1$) network ($N = 10$ neurons) that almost perfectly fits a bi-stable attractor ODE. Here, we compare our model against networks of the same size (and rank) trained using BPTT (both trained and tested against a set of trajectories simulated from task specific ODEs). As shown, our method provides a closed form solution in one step, as compared to networks trained with BPTT which take an order of one/two more magnitudes to converge. In Fig. 5, panels B,C depict loss curves across a wide range of RNN models trained with BPTT. Consistent with previous findings we observe lower training loss for larger networks, although they take longer to converge. Additionally, low-rank networks ($r = 1$, panel C) have comparable performance for tasks with lower dimensionality. Second, our method qualitatively has better reconstruction of test trajectories (panel A). More importantly, our model significantly outperforms networks (order of magnitude lower test mean-squared error) of the same size (and rank) on a set of test target trajectories (panel D), thereby proving the efficacy of our method.

7 Discussion

In this paper, we present an alternative view on low-rank RNNs that emphasizes interpretability and highlights the representational capacity of such networks. The focus of our work lies in defining a randomized basis which is used to embed an arbitrary non-linear dynamical system. Through a geometric portrait, we demonstrate that inputs are essential for capturing odd-symmetric functions. This extends previous work Valente et al. (2022); Dubreuil et al. (2022); Beiran et al. (2021) and offers clarifying insights into when such models behave as universal function approximators (similar to general RNNs). While previous work discusses universal approximation Beiran et al. (2021) for such networks, we believe we're the first to provide a geometric basis function interpretation.

Furthermore, our formulation allows learning the parameters of this RNN in closed form with regression. By directly modeling the low-dimensional activity and transforming to neural activity space via a fixed linear projection, we reduce the number of parameters needed to be learnt. We achieve this by presenting an NEF approach Eliasmith & Anderson (2003) to train low-rank RNNs (a result also highlighted in Beiran et al. (2021)). Our novelty lies in directly providing an intuition on the role each neuron plays in the low-rank RNN while also overcoming gradient-based training

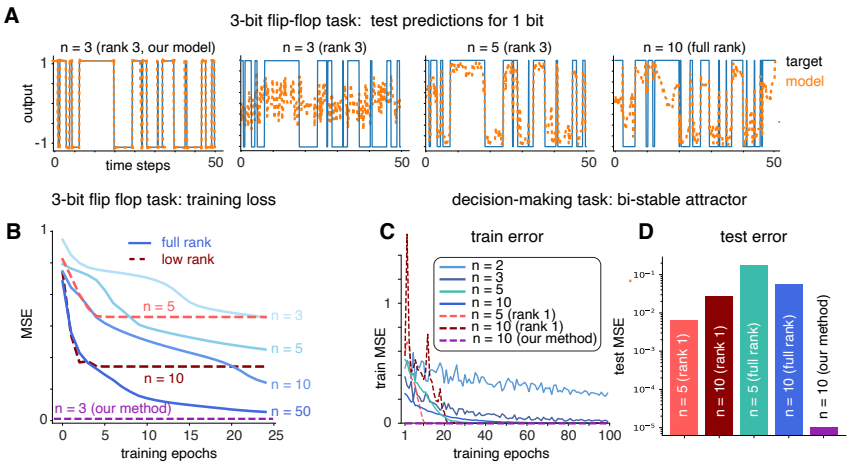

Figure 5: Comparisons to RNNs trained using backprop-through-time (BPTT) for neuroscience inspired tasks. **(A)** Target and trained RNN model outputs for one bit in the "3-bit flip-flop task". Our model (left) achieves near perfect accuracy using only 3 neurons and a rank-3 weight matrix; low rank and full rank networks trained using BPTT do not achieve nearly the same level of accuracy. **(B)** Training loss as a function of number of training epochs for different networks. (Our network, which is trained in one step using least-squares regression is shown in purple for comparison). **(C,D)** Train and test error for RNNs trained to perform a binary decision-making task using bi-stable attractor dynamics (Wong & Wang, 2006; Luo et al., 2023).

issues (in cases with known/estimated ODEs), similar to vector-field regression or teacher forcing algorithms Heinonen et al. (2018); Bhat et al. (2020); Hess et al. (2023). Our framework can thus be used as an alternative to task-training in neuroscience, to model novel behavioral tasks. Another exciting finding of our work is using OMP to approximate the smallest RNN (from a basis set), which could be used to drive insights on hyper-parameter values for such models. Together, this presents a promising future direction for studying how perturbing connectivity relates to unstudied behavioral outputs, or guiding experimentalists on capturing neurons with characteristic neural profiles (using OMP) for specific tasks.

We also present novel findings on the influence of input driven dynamics. Specifically, we directly link how non-autonomous ODEs can be embedded in low-rank RNNs through time-varying basis functions. Empirically, we demonstrate that identical trajectories can be generated from trajectories of moving fixed points, no fixed points or stationary target ODEs. The presence of dynamics in fixed points suggests a potential failure mode in current methods for interpreting such networks' dynamics Sussillo & Barak (2013); Smith et al. (2021). Furthermore, we link the RNN connectivity to these target ODEs through dynamics along the input dimension. A potential future direction would be to guide causal perturbation experiments needed to uncover such dynamics. Additionally, although not explored here, the conversion of non-autonomous dynamics to autonomous dynamics could play a critical role in neuroscientific insight. Lastly, we prove the efficacy of our method by applying it to various neuroscience inspired tasks. We note our method outperforms models of similar size/rank trained with BPTT.

We conclude by discussing some limitations of our work. Our method relies on knowing (or estimating via finite differencing methods) the underlying latent dynamic. Additionally, the complexity of our framework lies in defining or estimating this underlying ODE. While in Sec. 5 we provide instances of embedding non-autonomous ODEs, arguably extending this to other higher order systems could be tricky. This might be especially useful while modeling multi-region brain interactions, where the state of the target ODE depends on another complex dynamical system as well. However, overall we believe the new insights provided by our framework outweighs its limitations and provides an exciting set of future directions.

REFERENCES

Larry F Abbott, Brian DePasquale, and Raoul-Martin Memmesheimer. Building functional networks of spiking model neurons. *Nature neuroscience*, 19(3):350–355, 2016.

Alireza Alemi, Christian Machens, Sophie Deneve, and Jean-Jacques Slotine. Learning nonlinear dynamics in efficient, balanced spiking networks using local plasticity rules. In *Proceedings of the AAAI conference on artificial intelligence*, volume 32, 2018.

Omri Barak. Recurrent neural networks as versatile tools of neuroscience research. *Current opinion in neurobiology*, 46:1–6, 2017.

Omri Barak and Sandro Romani. Mapping low-dimensional dynamics to high-dimensional neural activity: A derivation of the ring model from the neural engineering framework. *Neural Computation*, 33(3):827–852, 2021.

Manuel Beiran, Alexis Dubreuil, Adrian Valente, Francesca Mastrogiuseppe, and Srdjan Ostojic. Shaping dynamics with multiple populations in low-rank recurrent networks. *Neural Computation*, 33(6):1572–1615, 2021.

Harish S Bhat, Majerle Reeves, and Ramin Raziperchikolaei. Estimating vector fields from noisy time series. In *2020 54th Asilomar Conference on Signals, Systems, and Computers*, pp. 599–606. IEEE, 2020.

Martin Boerlin, Christian K. Machens, and Sophie Denève. Predictive coding of dynamical variables in balanced spiking networks. *PLoS Comput Biol*, 9(11):e1003258, 11 2013. doi: 10.1371/journal.pcbi.1003258. URL `http://dx.doi.org/10.1371%2Fjournal.pcbi.1003258`.

Ricky TQ Chen, Yulia Rubanova, Jesse Bettencourt, and David K Duvenaud. Neural ordinary differential equations. *Advances in neural information processing systems*, 31, 2018.

Brian DePasquale, Christopher J. Cueva, Kanaka Rajan, G. Sean Escola, and L. F. Abbott. full-force: A target-based method for training recurrent networks. *PLOS ONE*, 13(2):1–18, 02 2018. doi: 10.1371/journal.pone.0191527. URL `https://doi.org/10.1371/journal.pone.0191527`.

Alexis Dubreuil, Adrian Valente, Manuel Beiran, Francesca Mastrogiuseppe, and Srdjan Ostojic. The role of population structure in computations through neural dynamics. *Nature neuroscience*, 25(6):783–794, 2022.

Lea Duncker and Maneesh Sahani. Dynamics on the manifold: Identifying computational dynamical activity from neural population recordings. *Current opinion in neurobiology*, 70:163–170, 2021.

Chris Eliasmith and Charles H Anderson. *Neural engineering: Computation, representation, and dynamics in neurobiological systems*. MIT press, 2003.

Aniruddh R Galgali, Maneesh Sahani, and Valerio Mante. Residual dynamics resolves recurrent contributions to neural computation. *Nature Neuroscience*, 26(2):326–338, 2023a.

Aniruddh R Galgali, Maneesh Sahani, and Valerio Mante. Residual dynamics resolves recurrent contributions to neural computation. *Nature Neuroscience*, 26(2):326–338, 2023b.

Markus Heinonen, Cagatay Yildiz, Henrik Mannerström, Jukka Intosalmi, and Harri Lähdesmäki. Learning unknown ode models with gaussian processes. In *International conference on machine learning*, pp. 1959–1968. PMLR, 2018.

Florian Hess, Zahra Monfared, Manuel Brenner, and Daniel Durstewitz. Generalized teacher forcing for learning chaotic dynamics. *arXiv preprint arXiv:2306.04406*, 2023.

Herbert Jaeger. The "echo state" approach to analysing and training recurrent neural networks. *Bonn, Germany: German National Research Center for Information Technology GMD Technical Report*, 148:34, 2001.

Ingmar Kanitscheider and Ila Fiete. Training recurrent networks to generate hypotheses about how the brain solves hard navigation problems. *Advances in Neural Information Processing Systems*, 30, 2017.

Christopher Langdon and Tatiana A Engel. Latent circuit inference from heterogeneous neural responses during cognitive tasks. *BioRxiv*, pp. 2022–01, 2022.

Timothy P Lillicrap and Adam Santoro. Backpropagation through time and the brain. *Current opinion in neurobiology*, 55:82–89, 2019.

Yuhan Helena Liu, Aristide Baratin, Jonathan Cornford, Stefan Mihalas, Eric Shea-Brown, and Guillaume Lajoie. How connectivity structure shapes rich and lazy learning in neural circuits. *arXiv preprint arXiv:2310.08513*, 2023.

Mantas Lukoševičius and Herbert Jaeger. Reservoir computing approaches to recurrent neural network training. *Computer science review*, 3(3):127–149, 2009.

Thomas Zhihao Luo, Timothy Doyeon Kim, Diksha Gupta, Adrian G Bondy, Charles D Kopec, Verity A Elliot, Brian DePasquale, and Carlos D Brody. Transitions in dynamical regime and neural mode underlie perceptual decision-making. *bioRxiv*, pp. 2023–10, 2023.

Wolfgang Maass, Thomas Natschläger, and Henry Markram. Real-time computing without stable states: A new framework for neural computation based on perturbations. *Neural Computation*, 14:2531–2560, 2002.

Valerio Mante, David Sussillo, Krishna V Shenoy, and William T Newsome. Context-dependent computation by recurrent dynamics in prefrontal cortex. *Nature*, 503(7474):78–84, 2013.

Francesca Mastrogiuseppe and Srdjan Ostojic. Linking connectivity, dynamics, and computations in low-rank recurrent neural networks. *Neuron*, 99(3):609–623, 2018.

Paul Miller, Carlos D Brody, Ranulfo Romo, and Xiao-Jing Wang. A recurrent network model of somatosensory parametric working memory in the prefrontal cortex. *Cerebral Cortex*, 13(11):1208–1218, 2003.

Matthijs Pals, A Erdem Sagtekin, Felix Pei, Manuel Gloeckler, and Jakob H Macke. Inferring stochastic low-rank recurrent neural networks from neural data. arxiv [cs. lg], 2024.

Barak A Pearlmutter. Dynamic recurrent neural networks. 1990.

Arthur Pellegrino, N Alex Cayco Gajic, and Angus Chadwick. Low tensor rank learning of neural dynamics. *Advances in Neural Information Processing Systems*, 36:11674–11702, 2023.

Eli Pollock and Mehrdad Jazayeri. Engineering recurrent neural networks from task-relevant manifolds and dynamics. *PLoS computational biology*, 16(8):e1008128, 2020.

William Qian, Jacob A Zavatone-Veth, Benjamin S Ruben, and Cengiz Pehlevan. Partial observation can induce mechanistic mismatches in data-constrained models of neural dynamics. *bioRxiv*, pp. 2024–05, 2024.

Kanaka Rajan, Christopher D Harvey, and David W Tank. Recurrent network models of sequence generation and memory. *Neuron*, 90(1):128–142, 2016.

Evan D Remington, Seth W Egger, Devika Narain, Jing Wang, and Mehrdad Jazayeri. A dynamical systems perspective on flexible motor timing. *Trends in cognitive sciences*, 22(10):938–952, 2018.

R. Schaeffer, M. Khona, L. Meshulam, International Brain Laboratory, and Ila R. Fiete. Reverse-engineering recurrent neural network solutions to a hierarchical inference task for mice. *bioRxiv*, pp. 2020–06, 2020.

Friedrich Schuessler, Francesca Mastrogiuseppe, Alexis Dubreuil, Srdjan Ostojic, and Omri Barak. The interplay between randomness and structure during learning in rnns. *Advances in neural information processing systems*, 33:13352–13362, 2020.

Jimmy Smith, Scott Linderman, and David Sussillo. Reverse engineering recurrent neural networks with jacobian switching linear dynamical systems. *Advances in Neural Information Processing Systems*, 34:16700–16713, 2021.

Terrence C Stewart. A technical overview of the neural engineering framework. *University of Waterloo*, 110, 2012.

David Sussillo. Neural circuits as computational dynamical systems. *Current opinion in neurobiology*, 25: 156–163, 2014.

David Sussillo and L. F. Abbott. Generating coherent patterns of activity from chaotic neural networks. *Neuron*, 63(4):544–557, Aug 2009. doi: 10.1016/j.neuron.2009.07.018. URL `http://dx.doi.org/10.1016/j.neuron.2009.07.018`.

David Sussillo and Omri Barak. Opening the black box: low-dimensional dynamics in high-dimensional recurrent neural networks. *Neural computation*, 25(3):626–649, 2013.

Elia Turner, Kabir V Dabholkar, and Omri Barak. Charting and navigating the space of solutions for recurrent neural networks. *Advances in Neural Information Processing Systems*, 34:25320–25333, 2021.

Adrian Valente, Jonathan W Pillow, and Srdjan Ostojic. Extracting computational mechanisms from neural data using low-rank rnns. *Advances in Neural Information Processing Systems*, 35:24072–24086, 2022.

Alex H Williams, Erin Kunz, Simon Kornblith, and Scott Linderman. Generalized shape metrics on neural representations. *Advances in Neural Information Processing Systems*, 34:4738–4750, 2021.

Kong-Fatt Wong and Xiao-Jing Wang. A recurrent network mechanism of time integration in perceptual decisions. *Journal of Neuroscience*, 26(4):1314–1328, 2006.

A APPENDIX A: CHOICE OF NONLINEARITY

If we consider a network with a rectified-linear instead of a $\tanh$ nonlinearity, the restrictions on the network's representational capacity in the absence of inputs are even more severe (Fig. SI-1). In this case, the basis functions are all scaled and axis-flipped *relu* functions that intersect the x axis at $x = 0$. Thus they can only represent piecewise linear functions composed of two pieces with a knot at zero. Adding inputs (or per-neuron biases) allows the network to have universal approximation capabilities.

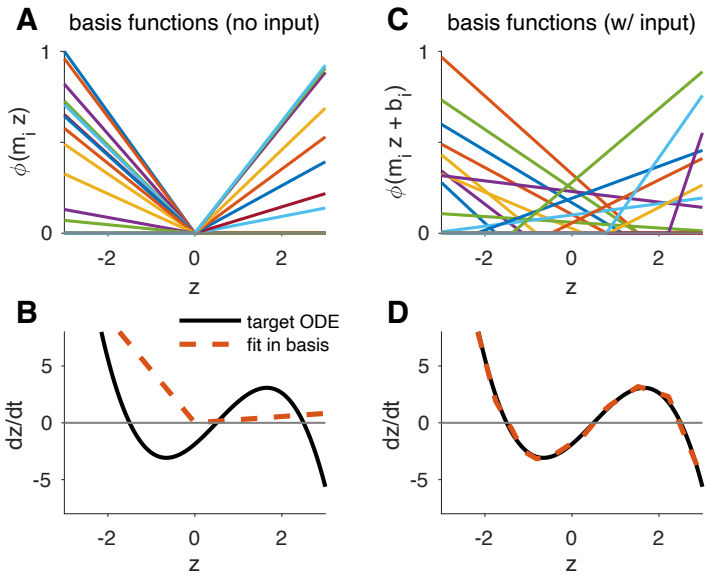

Figure SI-1: Representational capacity of a 1D low-rank RNN with rectified-linear (*relu*) nonlinearity. **(A)** Set of basis functions obtained by taking random coeffients $m_i \sim \mathcal{N}(0, 1)$ but without input ($\mathbf{v}_t = 0$). **(B)** Attempting to fit an example ODE using this basis recovers only a piecewise linear fit with a kink at zero. **(C)** By adding inputs, basis functions have random offset as well as slope. Here we set $\mathbf{v}_t = 1$ and sampled the input vector coefficients $I_i \sim \mathcal{N}(0, 1)$. **(D)** Least squares fitting of $\mathbf{n}$ in the random basis from (C) provides a high-accuracy approximation to the target ODE.

A.1 COMPARISON OF ACTIVATION FUNCTIONS IN ESTIMATING ODES

In this section, we explore the low-rank RNN's ability to approximate different types of dynamics (i.e function classes), with different activation functions (i.e basis functions). Our discussion above highlights how relu units can approximate functions through piecewise linear components. Non-zero inputs create basis functions which can be used to compose ODEs with "knots" at the shifted offsets. Alternatively, through our discussion in Section 3, we note tanh units provide smooth non-linear basis functions. The non-zero inputs create shifted basis functions, which perform a similar role, with smooth compositions. Following this intuition, if an ODE consists of smooth non-linear components it can be hypothesized that tanh units would have higher performance. Whereas, if the ODE consists of piecewise linear dynamics, relu units would prove to be more optimal. To validate this, we simulate two such ODEs in Fig. SI-2. Trivially, in the case of large enough number of basis functions, networks comprising of relu or tanh units can approximate any function (i.e they behave as universal approximators). However, to assess performance, we estimate the smallest networks in both cases that can fit the ODE within a pre-defined margin of error. As expected, the ODE with smoother non-linearities can be fit with smaller tanh networks than relu networks (the opposite is true for piecewise linear ODEs).

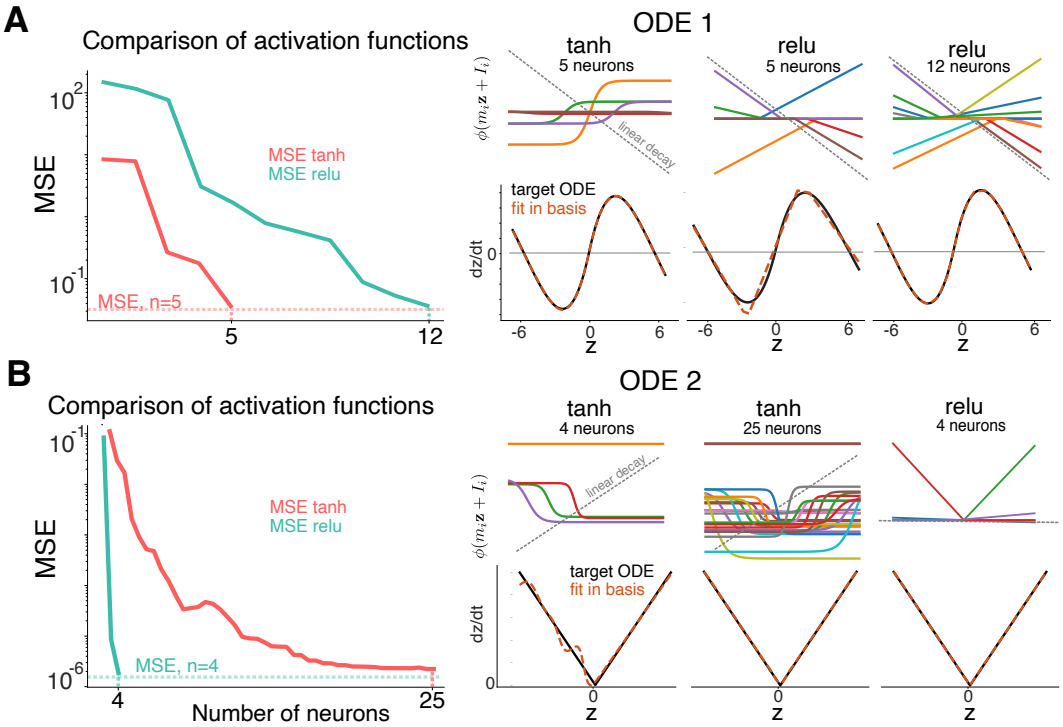

Figure SI-2: Performance comparison of tanh v/s relu in approximating different ODEs. **(A)** Depicts an ODE with two stable fixed points and one unstable fixed points. **(B)** Depicts an ODE with a shifted knot and two linear components. First column represents MSE (for a network with tanh and relu activations) as a function of the number of neurons in network. Neurons are added using OMP. Top row shows scaled basis functions selected after 1, 3, 5 iterations of OMP, along with the linear decay term $-x$. Bottom row shows target ODE (black) and RNN fit (orange) after each step of OMP.

A.2 Absence of inputs for limit cycle

Section 3.1 depicts a limit cycle embedded into the low-rank RNN using our framework. The specific ODE of our non-linear and non-symmetric system is give as -

$$\frac{dx}{dt} = \left(\frac{1-\left(z_0^2+z_1^2\right)}{\sqrt{z_0^2+z_1^2+\epsilon}}\right) z_0 - z_1 - 0.35$$

$$\frac{dy}{dt} = \left(\frac{1-\left(z_0^2+z_1^2\right)}{\sqrt{z_0^2+z_1^2+\epsilon}}\right) z_1 + z_0 + 0.5$$

where ϵ is a small constant added for numerical stability. The constant values in each dimension make the underlying ODE non odd-symmetric.

In this section we show the inability of an RNN without inputs to appropriately approximate this function. In Fig. SI-3, the first column represents contour plots of the target ODE for each dimension. The overlayed vertical and horizontal dashed red lines depict $X = z_1 = 0, Y = z_2 = 0$ respectively. Note, there is a slight (left and upwards) shift in the contour plots, indicating the non-radial symmetry. This is introduced by adding a constant negative decay in z_1 and a positive correction in z_2. The second column represented the fitted ODEs for an RNN with inputs, while the last column represents fitted ODEs for an RNN without inputs. It can be observed the RNN without inputs is unable to create offsets in any dimension, thus failing at recovering the underlying ODE. To further highlight this we simulate a sample trajectory from the polar coordinates of a limit cycle (detailed in Section 3.1) in the last row of Fig. SI-3. As expected, the low-rank RNN with inputs almost perfectly overlaps the trajectory, unlike the low-rank RNN without inputs.

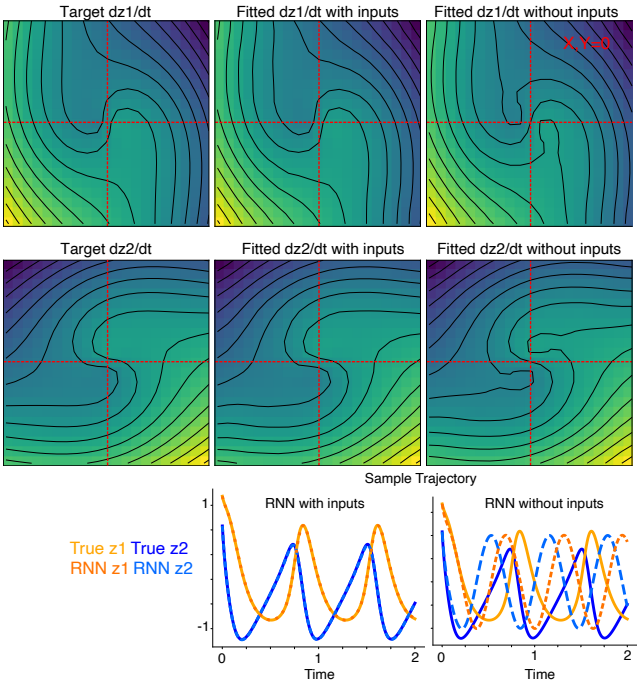

Figure SI-3: Influence of inputs in capturing non-symmetrical limit cycle

B General Formulation and Application To Binary Decision Making Task

We apply our framework to a specific group of binary decision making tasks commonly observed in systems neuroscience. In this task, a rat accumulates evidence of auditory pulses over time from clicks on its left and right side. At the end of the stimulus period, the rat must turn to the side which produced more clicks, and is rewarded for inferring this correctly. It has been shown that multiple underlying dynamical portraits could represent this behavior Luo et al. (2023). We thus show applicability of our method by using it to recover the intrinsic and input driven dynamics on four separate synthetically generated dynamic portraits linked to this task Luo et al. (2023). Here, intuitively, the input dynamics encode for the accumulation of evidence based on the clicks, and a final decision to turn is made once the accumulation value reaches a specific attractor in the network. For instance, if the instrinsic dynamics encode a bi-stable attractor, each of the end points represent a specific decision, and the inputs move the dynamics along a line between them Wong & Wang (2006). Additionally, consistent with previous studies, we model our simulations to provide equal weights to left and right clicks but with opposite magnitudes.

We model four flow fields representing intrinsic dynamics, namely a bi-stable attractor, a line attractor, an non-canonical line attractor and the flow field inferred from Luo et al. (2023). More formally, they are given as follows -

Bistable attractors:

$$dz_1 = 10z_1(0.7 + z_1)(0.7 - z_1)dt + cudt$$
$$dz_2 = -10z_2dt$$

Classic DDM - line attractor:

$$dz_1 = \begin{cases} cudt & z_1 \in (-0.7, 0.7) \\ 10z_1(0.7 - z_1)(0.7 + z_1)dt & z_1 \notin (-0.7, 0.7) \end{cases}$$
$$dz_2 = -30z_2 \tag{15}$$

Non-canonical line attractor:

$$dz_1 = 5z_2$$
$$dz_2 = -5z_2dt + cudt$$

Unsupervised model:

$$dz_1 = 5z_1(0.85 + z_1)(0.85 - z_1)dt + cudt$$
$$dz_2 = 5(0.5|z_1| + 0.1)(z_1 - 1.2z_2)$$

Here, z_1, z_2, represent the two latent dimensions, u represents the magnitude of the input clicks, and c represents if its positive or negative.

Critically, we observe the input dynamics lie in a dimension *parallel* to the recurrent activity. Or alternatively, drive the system in the dimensionality spanned by the recurrent activity. We thus present a general formulation of our equations to model these input dynamics. Following Eqn 6, we now not only observe orthogonal ($I = I_{perp}$) neuron specific inputs, but additional input dynamics that influence the recurrent activity (I_{par}, spans the same direction as $\mathbf{m}$), thus updating Eqn 6 as :

$$\mathbf{x}(t) = \mathbf{m}\mathbf{z}(t) + I_{par}\mathbf{v}'(t) + I_{perp}\mathbf{v}(t), \tag{16}$$

Our goal of embedding the ODE $g(\mathbf{z})$ into the network can now be viewed as setting the model parameters so that

$$g(\mathbf{z}) + \mathbf{z} \approx \mathbf{n}^\top \phi(\mathbf{m}\mathbf{z} + I_{par}\mathbf{v}'(t) + I_{perp}\mathbf{v}(t)) \tag{17}$$

where $\mathbf{v}'(t)$ represents the low-pass filtered input which drives the system in the dimensions spanned by the recurrence ($\mathbf{m}$). This allows us to follow a similar setup to our discussions in Sec. 3, with the exception that auditory inputs are applied along I_{par} or $I = I_{perp}$, or both.

As shown in Fig SI-4, each row represents one of the above dynamical regimes. The first column represents the dynamics along z_1, or z_2, and the RNN fitted version. Next, we model two right (or positive) clicks at $t = 0.5$ and $t = 1$ second and a single left (negative) click at $t = 2.5$ second. The second column represents the ODE when we start from ($z = 0$), pushed by these input dynamics, for our fitted RNN dynamics (Eqn 7) against the true ODE (computed using Euler method). Lastly, we also recover the underlying flow fields, as indicated by the last column. In Fig SI-5, we embed a non-canonical line-attractor in which input axis is perpendicular to the line attractor and non-normal dynamics give rise to movement along the line attractor. We successfully embedded all three of these systems with rank 1 RNNs. Lastly, we also embed a system with rotational dynamics between fixed points with integration along the diagonal between them. This is done through a rank 2 RNN with inputs along each of the directions spanned by I_{par}(Fig. SI-5 B). This proves the flexibility of our framework in embedding dynamics associated with neuroscience tasks.

C Additional Tasks and Comparisons

C.1 Discussion on FORCE Framework

Below we discuss some ways in which our methodology differs from the FORCE/FULL-FORCE (Sussillo & Abbott, 2009; DePasquale et al., 2018) training schemes.

1. **Initialization with Full-Rank Weight Matrix:** FORCE/FULL-FORCE methods require full rank-initializations, and learn low-rank updates on this initilalization over time. This comes at the cost of interpretibility as the dynamics of such networks need to be analysed post training through methods such as PCA. On the other hand, our framework directly models the latent low-dimensional dynamic and doesn't ever need full-rank initializations and is highly interpretable.

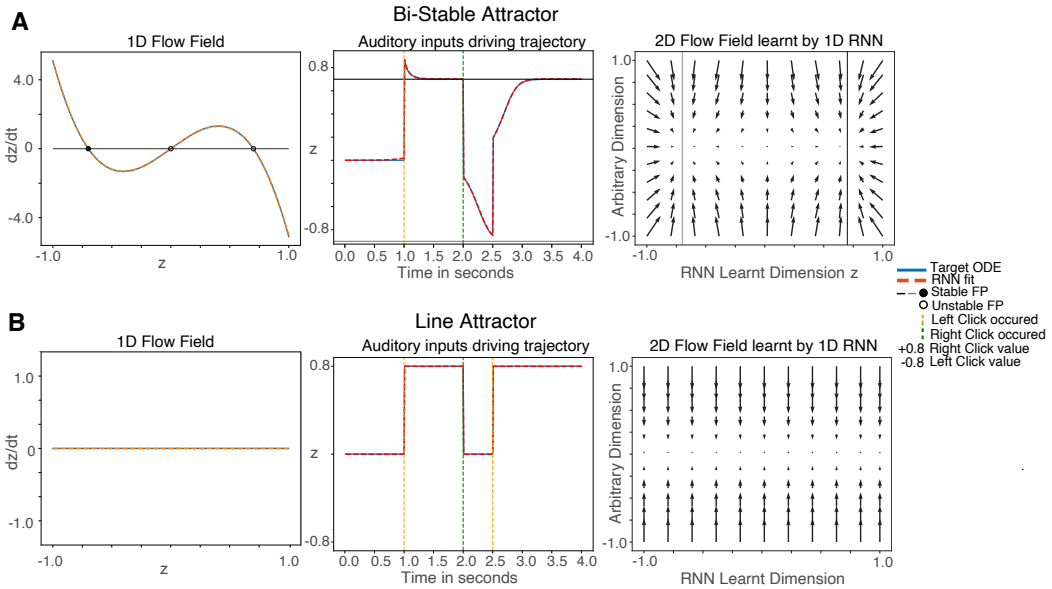

Figure SI-4: Two different dynamical portraits for binary decision making task: **(A)** bi-stable attractor ODE and **(B)** line attractor ODE. First column represents the true underlying ODE and the RNN estimate learned using least squares. Second column depicts a sample trajectory driven by momentary input clicks. A right click creates a drift towards the positive stable fixed point where as a left click, towards the negative stable fixed point for A. For B, accumulation along the line takes place with no diffusion. Third column represents the flow-field estimated by the RNN.

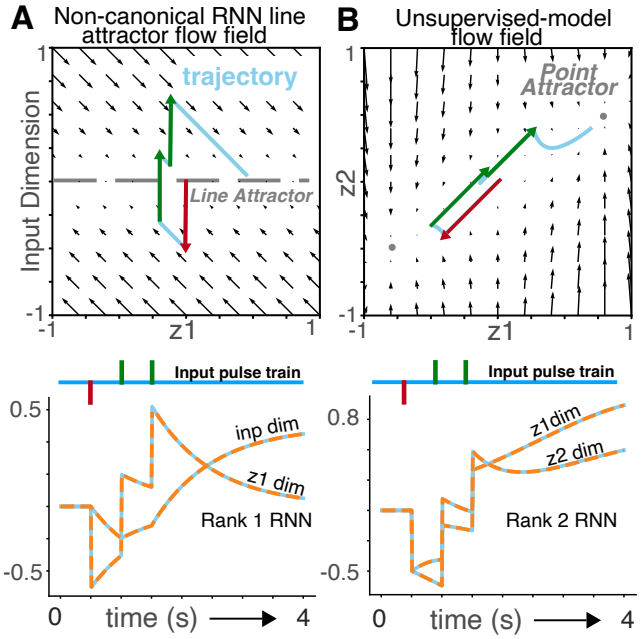

Figure SI-5: Two additional dynamical portraits for binary decision making task. Top: flow-field for each ODE, with input driven trajectory highlighted in blue. Bottom: true and fitted trajectories over time for each dimension.

2. **Senstive to initialization and requires multiple epochs:** One of the motivations of FORCE is that it introduces the benefits of training networks that exhibit chaotic activity prior to training. While powerful, it is observed this results in these networks needing multiple epochs/iterations. Additionally, these networks exhibit stochastic results based on initialization. In contrast, our method provides a deterministic and single-step closed form solution.
3. **Doesn't Directly Embed an ODE, but Produces a Set of Target Trajectories:** A stark difference between our framework is unlike other training methodologies similar to FORCE and FULL-FORCE that are trained against target trajectories, we can also directly model the underlying ODE. Thus, in cases where such a hypothesized ODE exists, we can represent the entire space of the low-dimensional dynamic.

C.2 3D Lorenz Attractor

In addition to the 1-dimensional and 2-dimensional ODEs described in the main text, we also scale our method to the Lorenz attractor. Specifically, we train our network on the Lorenz attractor over a set of 10 separate trajectories (start location denoted by red circles in Fig SI-6). Additionally, the error plots in Fig SI-6 indicates our network learns an accurate representation of this system.
Our formulation follows from our descriptions in Sec. 3.1, with one extra dimension. This can be formalized as a rank-3 RNN, written as the problem of fitting three different nonlinear functions $g_1(\mathbf{z})$, $g_2(\mathbf{z})$ and $g_3(\mathbf{z})$ using three different linear combinations of the same 3D basis functions:

$$g(\mathbf{z}) = \begin{bmatrix} g_1(\mathbf{z}) \\ g_2(\mathbf{z}) \\ g_3(\mathbf{z}) \end{bmatrix} \approx -\begin{bmatrix} z_1 \\ z_2 \\ z_3 \end{bmatrix} + \begin{bmatrix} \mathbf{n}_1^\top \phi(M\mathbf{z} + I) \\ \mathbf{n}_2^\top \phi(M\mathbf{z} + I) \\ \mathbf{n}_3^\top \phi(M\mathbf{z} + I) \end{bmatrix}, \tag{18}$$

where $M = [\mathbf{m}_1 \mathbf{m}_2 \mathbf{m}_2]$ is a $d \times 3$ matrix, I is once again a column vector of offsets, and we have assumed a constant filtered input, $\mathbf{v} = 1$.

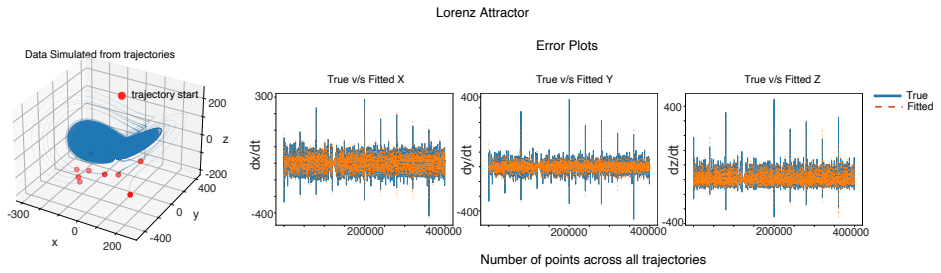

Figure SI-6: Lorenz attractor

Lastly, in Fig SI-7) we also show the efficacy of our model on a sample test trajectory. As shown, our low-rank RNN model recovers the time-traces with high accuracy.

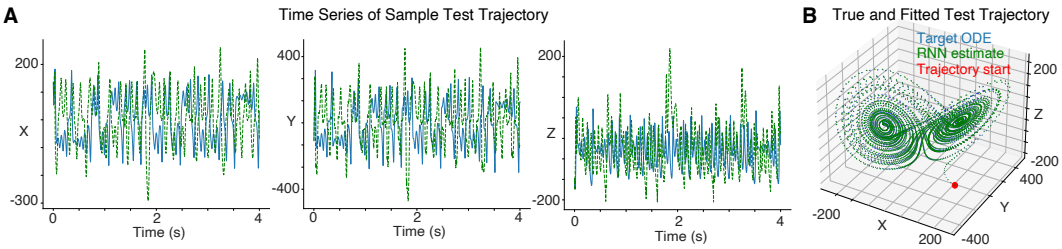

Figure SI-7: Performance on sample test trajectory

D OMP FOR 2D LIMIT CYCLE

Following our discussion on the multi-dimensional case and OMP (Sec. 3.1 and 4), we apply our framework to learn the smallest number of neurons needed to fit an RNN for the limit cycle ODE. As depicted in Fig SI-8), with the addition of neurons we start noticing periodicity in trajectories with just 6 neurons. Finally, we obtain near perfect fits with 20 neurons.

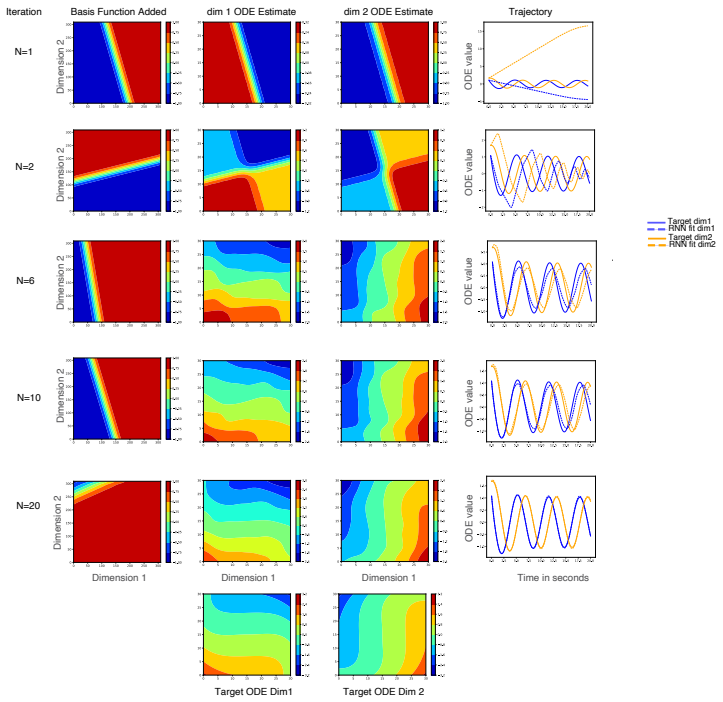

Figure SI-8: OMP for 2d Limit Cycle. Column 1 shows the single basis function added the corresponding iteration of OMP. Columns 2 and 3 represent the estimated flow-fields via a learnt linear weight, i.e two separate weights are learnt using the same basis function. Last column depicts a sample trajectory. Note, periodicity of the limit cycle starts appearing as more neurons are added.

E PARAMETER DISTRIBUTION OF RANDOM BASIS

In this section we delve into the role of the distribution from which the random basis is sampled. As shown in Section 4, each basis function approximates the ODE ($g(\mathbf{z})$) over some finite domain ($\mathbf{z}$). Thus, first, it is critical the basis functions span the domain of the function being approximated. Second, these functions need not be odd symmetric and hence basis functions need to also be shifted to capture these movements. As shown in Fig SI-9), as long as these properties are met (i.e both the uniform grid and standard normal generate basis functions in the same domain, with the same offset ranges), the exact underlying distribution from which the basis functions are drawn does not play a critical role. This can be seen as the MSE values follow similar trends with greedy addition of basis functions (panel C). Qualitatively, this can also be observed via similar reconstruction of the ODE across iterations of OMP (panel A,B).

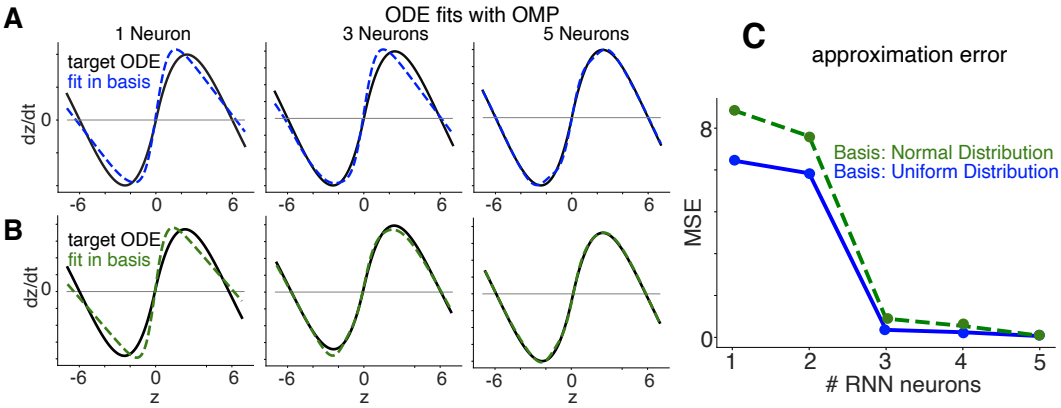

Figure SI-9: Influence of distribution of basis functions. **(A,B)** RNN estimated fit of Bi-stable attractor ODE the true underlying ODE over 1,3,5 iterations of OMP. In the top row basis functions (both m_i and I_i) are generated over a uniform grid spanning $+1$ to -1. Alternatively the bottom row consists of basis functions generated from a standard normal (i.e $m_i \sim \mathcal{N}(0,1)$, and $I_i \sim \mathcal{N}(0,1)$). **(C)** Mean squared error (MSE) between target ODE and RNN approximation as a function of the number of RNN neurons added by OMP (blue: basis functions drawn from uniform grid, green: basis functions drawn from standard normal).

F Additional Training Details

In Section 6, both our framework and the networks trained with BPTT are trained from a set of teacher trajectories, which are simulated from the underlying ODE (eg. for binary decision making - they start somewhere on the grid and eventually converge to one of the two fixed points). However, unlike previous sections, our method here can be broken into two main steps -

1. **Estimate ODE**: Through a finite differencing approach (euler), we compute the difference between every pair of points along the training trajectory. Thus, using a small time bin, we estimate the value of $g(\mathbf{z})$ along each point of the trajectory. This is used to populate our target vector for regression.
2. **Perform Regression:** Our basis matrix is evaluated at grid points along these training trajectories. Given this design matrix, and target we compute the necessary weights through Eqn 9.

Lastly, both our framework and the networks trained with BPTT must reproduce a set of target trajectories (eg. blue lines in In Fig. 5, panel A) from an input pulse train (eg. representing bit value for each channel over the time interval). Thus, both our method and models trained with gradient methods are trained to uncover underlying dynamics (from data points) that solve the task.

As shown in Table 1, 2, our framework provides significantly faster training.

Table 1: Training Time For Binary-Decision Making Task

Model Type	Size	Time(s)
Low Rank ($r = 1$)	5	62.419
Low Rank ($r = 1$)	10	62.468
Full Rank	2	29.161
Full Rank	3	29.209
Full Rank	5	29.025
Full Rank	10	29.392
Full Rank	50	28.998
Our Model	5	0.069

Table 2: Training Time For 3-Bit Flip Flop Task

Model Type	Size	Time(s)
Low Rank ($r = 3$)	5	305.256
Low Rank ($r = 3$)	10	303.559
Full Rank	3	170.512
Full Rank	5	169.076
Full Rank	10	170.239
Full Rank	50	173.590
Our Model	5	0.09

F.1 Application to high dimensional noisy data

We further validate our framework by discussing its application to high-dimensional noisy data. In this case we assume we have access to high-dimensional noisy rate-based neural recordings. Specifically, this simulation is achieved by simulating a trajectory from the bi-stable ODE in Fig. SI-5 B. This trajectory $\mathbf{z}(t)$, starts somewhere on the grid of $\mathbf{z}$, and is run forward until it converges to one of the fixed points. To convert this into a high-dimensional noisy rate based recordings we take the following steps. For each value along this trajectory $\mathbf{z}(t)$ we -

1. Project it into a high dimensional space through a linear weight matrix (values are drawn between 0-1).
2. This linear mapping is made non-linear via the $\tanh$ activation
3. Finally, we independently add Gaussian noise to each of the dimensions ($\mathcal{N}(0, 0.01)$).

We thus assume we have access to these high-dimensional recordings. We project the data onto the top PC's(since the underlying dynamic here is 1-d, the first PC dimension captures the dynamic). In Fig. SI-10, the low-dimensional trajectory was first projected into a 1000 dimensional space. PCA on this trajectory showed the single top PC captured most of the variance in the data. As shown, through this projection we recover a noisy trajectory that represents the true low-dimensional dynamic. The rank of the network will depend on the number of PC dimensions needed, in this case 1 suffices. Furthermore, as noise in the system increases this recovery will also become more noisy (or need more dimensions to capture it). Other confounding factors such as low-resolution recordings or sparse recordings could also influence recovery (although not explored here).

Finally, once we have access to these trajectories the approach discussed in Section F can once again be followed.

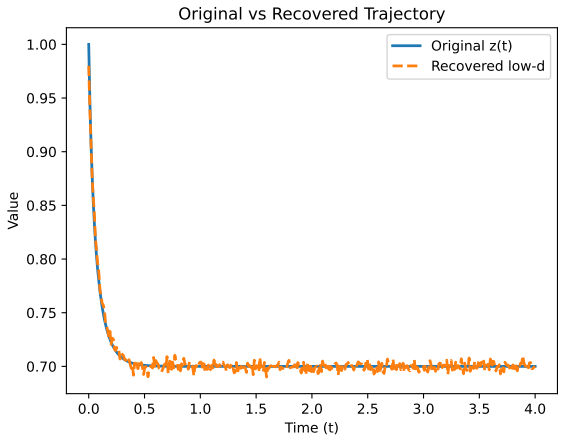

Figure SI-10: Recovering low-dimensional trajectory from noisy dimensional data